Powder Technology 402 (2022) 117355

Contents lists available at ScienceDirect

Powder Technology

journal homepage: www.elsevier.com/locate/powtec

Powder-flow behavior and process mechanism in laser directed energy deposition based on determined restitution coefficient from inverse modeling

Yanhua Bian [a,c,d], Xiuli He [a,c,*], Gang Yu [a,b,c,*], Shaoxia Li [a,c], Chongxin Tian [a,c], Zhiyong Li [a,c], Yanmei Zhang [a,c], Junming Liu [d]

[a] Institute of Mechanics, Chinese Academy of Sciences, Beijing 100190, China
[b] Center of Materials Science and Optoelectronics Engineering, University of Chinese Academy of Sciences, Beijing 100049, China
[c] School of Engineering Science, University of Chinese Academy of Sciences, Beijing 100049, China
[d] Research Institute of 3D Printing, Beijing City University, Beijing 100083, China

ARTICLE INFO

Article history:
Received 13 January 2022
Received in revised form 26 March 2022
Accepted 28 March 2022
Available online 4 April 2022

Keywords:
Laser directed energy deposition
Computational fluid dynamics
Powder-flow behavior
Restitution coefficient
Inverse modeling

ABSTRACT

In order to clarify the transportation mechanism of particles in continuous coaxial powder feeding (CCPF) process, a trial-and-matching method is developed to quantify the restitution coefficient which is used to describe the inelastic collision between the particle and the nozzle wall. The consistency of the outlet velocity and the spatial concentration distribution of particles between the experimental statistic and the numerical calculation shows that the restitution coefficient of 0.9 can be used to measure the inelastic collision behavior between particles and the nozzle wall. Employing the determined restitution coefficient, a semi-quantitative method based on optical diagnostic and quantitative analysis derived from numerical calculation are proposed to study the powder-gas flow transport characteristics from single-layer to multi-layer jet flow. It is found that the outer shielding gas flow (OSGF) has a great influence on the multi-layer jet flow field, and it is most conducive to powder focusing at the OSGF of 20 L/min. The velocity distribution of CGF determined by the inner structure of CCPFN and the inelastic collision between the particle and the wall are the two mutually coupled factors that determine the outlet velocity of particles. Frequent inelastic collisions and the decrease of the CGF velocity lead to velocity dispersion and trajectory fluctuation of particles. When the inlet velocity of particles is 1.33 m/s, the outlet velocity ranged from 0.4 m/s to 0.9 m/s. This paper aims to provide a general method to determine the restitution coefficient and offer a comprehensive understanding of transportation mechanism of power particles both inside continuous coaxial powder feeding nozzle (CCPFN) and multi-layer jet zone between substrate and the CCPFN outlet.

1. Introduction

Laser directed energy deposition (LDED) with the production mode of adding material is a promising technology, which is capable of manufacturing wear-resistant coatings [1], composite parts [2], functionally graded components [3] and repairing parts [4]. In LDED process, a laser is focused on the substrate and then the substrate melts. In the meantime, the powder is transported to the molten pool by pneumatic transportation. Through the rapid melting and solidification process, metallurgical bonding layer is formed between substrate and additive materials [5,6]. Stable and controllable powder feeding is of great importance to achieve smooth surface and defect-free manufactured parts or deposited layer [7]. Continuous coaxial powder feeding (CCPF) is the most widely used method to transport particle materials. Powder jet with circular distribution can be achieved by using continuous coaxial powder feeding nozzle (CCPFN), which consists of an annular wedge-shaped channel. Powders are transmitted in the wedge-shaped channel under the drag force of single-layer jet of carrying gas flow (CGF). After several collisions between particles and the wedge-shaped wall, the particles are emitted from the CCPFN, and spatial concentration distribution can be formed between substrate and the CCPFN outlet. There are also other two kinds of shielding gas flow in CCPF process, namely, the inner shielding gas flow (ISGF) and the outer shielding gas flow (OSGF). The ISGF is emitted from the center of the CCPFN, protecting the lenses from the powder particles rebounding from the substrate. The OSGF is emitted from the periphery of the powder flow

* **Corresponding authors at:** Institute of Mechanics, Chinese Academy of Sciences, Beijing 100190, China.
E-mail addresses: xlhe@imech.ac.cn (X. He), gyu@imech.ac.cn (G. Yu).

https://doi.org/10.1016/j.powtec.2022.117355
0032-5910/

to prevent powder particles and deposited layer from oxidation. When the powder is ejected from the CCPFN, the velocity and the trajectory of particles are affected by the coupling effect of multi-layer jet flow.

The outlet velocity of particles just ejected from the CCPFN is an important feature of powder transport behavior, which determines the transportation trajectory and spatial concentration distribution of particles in multi-layer jet zone. Moreover, the powder transport behaviors in space between the CCPFN and the subtract not only dominate the mass of powder particles reaching the melt pool and the thermal state of those particles, but also determine the laser power attenuation [8]. So it is very necessary to clarify the process mechanisms of the gas-powder flow from single-layer to multi-layer jet in CCPF process. Most researchers have carried out extensive studies [9–15] on transportation mechanisms of particles in CCPF process based on simulation and optical diagnostic methods. Lin et al. [9] studied powder flow under various arrangements of the nozzle exit through 2D simulation. It was found that a higher powder concentration can be achieved through a specific nozzle arrangement. The influence of two nozzle exits on the powder concentration was studied without considering the whole wedge structure. Zhang et al. [10] built a 2D axisymmetric model to investigate the concentration distribution and then suggested an optimal shielding gas flow. Zhu et al. [11] used gas-solid two-phase flow theory to build 2D axisymmetric model of coaxial powder feeding flow field. The effect of deposited layers and focus distance from nozzle outlet to convergence point on the powder concentration distribution was studied. From the view of whole CCPFN structure, the CCPFN is not completely symmetrical and the gas turbulence occurs in the whole three-dimensional space. Furthermore, the particles move along the three-dimensional trajectory. Hence, 3D simulation method is more suitable for the research of particle transport trajectories and spatial concentration distribution. Tabernero et al. [12] employed the turbulence k-ε model and the Euler-Lagrange approximation to simulate the powder flux distribution. The simulation results were confirmed by selective weight measuring method. In reference [13], the computational fluid dynamics (CFD) method was used to study particle trajectories and the interaction between particles and laser. Zhang et al. [14] investigated the effect of environment pressure and nozzle dimensions on distribution and velocity of particles. It was found that the nozzle dimensions have significant effect on particle distribution and velocity. Zhang et al. [15] established a 3D numerical model to analyze the aerodynamics characteristics and particle transport behavior of the nozzle. The results showed that the gas dynamic characteristic of the nozzle is the key factor affecting the powder flow field. In above research [12–15], the OSGF channel for the CCPFN used was neglected, which has important effect on the trajectory of particles ejected from the nozzle actually.

In the process of particle transportation, the trajectories of particles leaving the nozzle are strongly influenced by their collision behaviors and cannot be predicted accurately from the passage angles only through trigonometry and geometrical methods [16]. Moreover, the collision process between particles and wall is actually inelastic, and accompanied with the kinetic energy loss of particles. However, the effect of inelastic collision between the particles and the nozzle walls on the profile of particle transportation behavior was not included in the above study [9–15].

Generally, restitution coefficient, defined as the ratio of velocity before and after collision, is used to describe the inelastic collision process [17–21]. Pan et al. [17] developed a 3D stochastic non-spherical particle collision model for simulating the dispersion behavior of powder particles in and out the CCPFN. In this work, the effect of carrying gas and shielding gas on the spatial concentration of particles were not taken into consideration. Kovalev et al. [18,19] numerically investigated mechanisms of elastic and non-elastic reflection of the particles from the nozzle walls. They found that collisions of particles and walls of the transport channel impose the governing effect on the particle trajectories. There is only a comparative study of powder motion trajectories under two restitution coefficients and there is no theoretical guidance for the determination of the restitution coefficient. It was found in reference [20] that the powder concentration in the focus plane increases with the decrease of restitution coefficient by means of simulation. Li et al. [21] studied the incident direction and concentration distribution of powders for discontinuous coaxial powder feeding head. It was found that the collision of the powders with the inner wall of the passage is the reason for the powder stream divergence at the nozzle outlet. Notably, all the above studies on particle-wall collision were lack of experimental verification.

Optical diagnosis and image processing technology are important means to study particle behavior in CCPF process. Tan et al. [22] developed a photographic system to describe the powder feeding behaviors based on the powder flow images. In reference [23], schlieren-imaging, high-speed imaging and laser doppler anemometry were used for optical diagnostics of the flows. Wu et al. [24] developed a general powder distribution model based on an image-based powder measurement (IBPM) technique. Sergachev et al. [25] developed a noncontact registration methods to measure particle velocity and temperature in a coaxial jet gas flow.

In summary, there are two main problems to be addressed in studying powder transport behavior. First, the transportation behavior of powders in the CCPFN is determined by the mutual effect of drag force exerted by CGF and the inelastic collision between particles and the wall, which cannot be observed directly. Secondly, the restitution coefficient characterizing inelastic collision between particles and the inner wall of CCPFN cannot be accurately determined. This is due to the diversity of particle size distribution, particle morphology, the continuous changes of incident angle and velocity in the process of collision. As a result, the restitution coefficient cannot be specified by a single scientific principle. Hence, it is urgent to establish a model that can be used to deeply elaborate the powder transport behavior, including the physical processes of the interaction between particles and gas jet flow, the collision behavior between particles and the nozzle wall, and the impact of multi-layer jets on powder transport.

In this paper, experiments for capturing the exit behavior of particles and experiments for recording the transport morphology of particles are carried out to study the powder feeding behavior. Outlet velocity distribution of particles and semi-quantitative spatial mass concentration distribution are studied by using optical diagnosis and particle tracking method. Subsequently, a 3D computational fluid dynamics (CFD)- discrete phase model (DPM) coupling model for pneumatic transport of particles in CCPF process is built. The trial-and-matching method for experimental and numerical outlet velocity distribution of particles and spatial concentration is used to determine the restitution coefficient. Based on the determined restitution coefficient, dynamic pneumatic transportation characteristics, spatial concentration distribution controlled by OSGF are studied. Finally, the turbulence characteristics of jet flow from single-layer to multi-layer are analyzed quantitatively. This paper aims to provide a general method to determine the restitution coefficient and offer a comprehensive understanding of transportation mechanism of powder particles both inside CCPF and multilayer jet zone.

2. Experimental method

2.1. Nozzle structure

As shown in Fig. 1(a), a copper machined CCPFN consisting of three gas flow channel, namely the inner shielding gas flow (ISGF) channel, the carrying gas flow (CGF) channel and the outer shielding gas flow (OSGF) channel, was used in this study and its two-dimensional diagram was shown in Fig. 1(b). The structure tagged in red was the channel for cooling water, which was used to dissipate heat of the CCPFN. The detailed structure parameters were shown in Table 1.

The coordinate system (x, y, z) established based on the structure of the CCPFN was shown in Fig. 1(c). The center point O of the horizontal

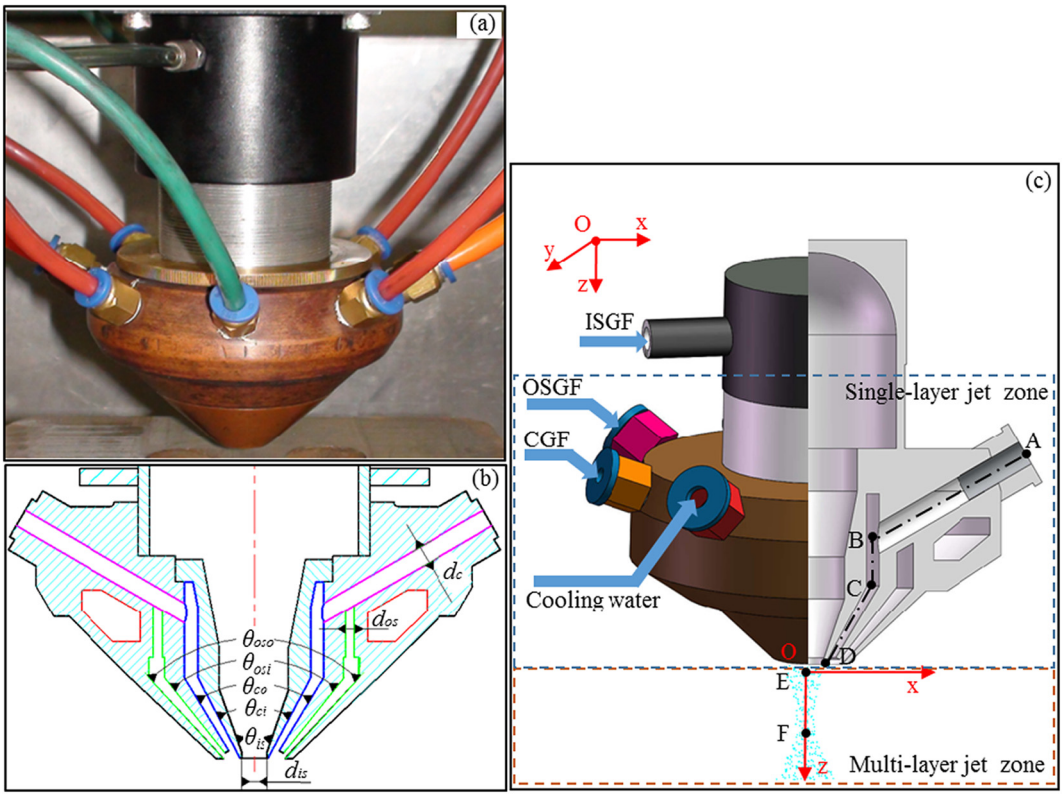

Fig. 1. Structure of CCPFN (a) Actual CCPFN (b) Two-dimensional diagram (c) Coordinate system established in CCPFN.

section of the CCPFN outlet was the origin of the coordinate system, and the central section along the gravity direction of the CGF channel was established as the Oxz plane. The horizontal plane of the powder-gas flow outlet was defined as the Oxy plane. The transportation behaviors of powder-gas flow from multi-layer jet to single-layer jet can be discussed clearly.

2.2. Process for observing the powder transportation

The method of optical diagnosis provides an intuitive and qualitative analysis for studying the transportation behavior of powders in LDED process. Combined with the image processing method, the particle transportation behavior (such as velocity and concentration of particles) can be obtained from the optical diagnosis image. In this study, two groups of experiments were carried out to study the powder feeding behavior, namely, experiments for capturing the exit behavior of particles and experiments for recording the transport morphology of particles.

In the experiments of capturing the exit behavior of particles, both the ISGF and OSGF were set to zero to ensure that the exit state of particles was only affected by CGF and inelastic collision. Detailed parameters in the powder feeding process were shown in Table 2. In the experiments of recording the transport morphology of particles, the ISGF and CGF were fixed during the experiments, and the transport morphology of particles was only affected by OSGF and the detailed processing parameters were shown in Table 3.

In this paper, a high-speed photography system (shown as Fig. 2) was developed to capture the powder transportation behavior. It consisted of a pneumatic powder feeder, a quadruple coincidence set, two strong LED light sources, a high-speed camera(i-speed210, iX Cameras, United Kingdom), and a CCPFN with its support frame. The high-speed camera was placed perpendicular to the symmetrical plane of inlet. The two strong LED light sources provided light for the whole powder flow field from two symmetrical positions, which was

Table 1
Structure parameters of CCPFN.

Variable	Symbol	Value
ISGF inlet diameter	d_{is}	6 mm
OSGF inlet diameter	d_{os}	4 mm
CGF inlet diameter	d_c	4 mm
ISGF channel angle	θ_{is}	38.5°
CGF channel inner angle	θ_{ci}	55.5°
CGF channel outer angle	θ_{co}	62.5°
OSGF channel inner angle	θ_{osi}	77.0°
OSGF channel outer angle	θ_{oso}	85°
Number of CSGF inlet		4
Number of OSGF inlet		2

Table 2
Process parameters in capturing the exit behavior of particles.

Variable	Value
ISGF rate	0 L/min
OSGF rate	0 L/min
CGF rate	4 L/min
Powder feeding rate	30 g/min
Type of protective gas	argon

Table 3
Process parameters in recording the transport morphology of particles.

Variable	Value
ISGF rate	10 L/min
OSGF rate	0,5,10,15,20,30 L/min
CGF rate	4 L/min
Powder feeding rate	30 g/min
Type of protective gas	argon

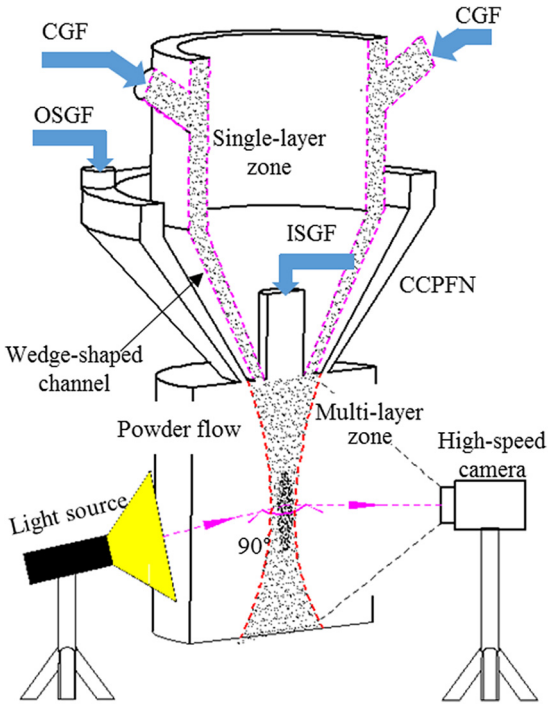

Fig. 2. Schematic diagram for capturing spatial morphology of powders.

perpendicular to the shooting direction of high-speed camera. In the experiments of capturing the exit behavior of particles, the high-speed camera was set with the frame rate of 1500 per second, the frame size of 992 × 540 and the exposure time of 80 ms. In the experiments of recording the transport morphology of particles, the high-speed camera was set with the frame rate of 1500 per second, the frame size of 768 × 1710 and the exposure time of 300 ms.

2.3. Material

Gas atomized, near-spherical 316 L powders were used in this study. For an accurate simulation of the particle characteristics, the size distributions of the powders were studied by scanning electron microscope (SEM) and sieve analysis. The morphology of the powders was shown in Fig. 3 and the particle size by sieve analysis was shown in Table 4. As shown in eq. (1), shape factor ϕ_s is employed to describe the proximity of particle shape to sphere.

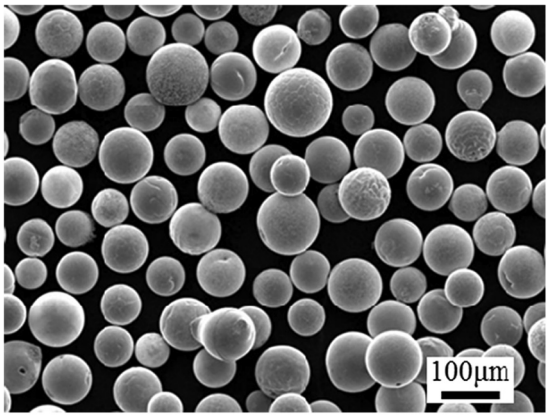

Fig. 3. Morphology of 316 L particles.

Table 4
Size distribution of 316 L particles.

Parameters	Value
Minimum diameter(μm)	48.09
Maximum diameter(μm)	157.71
Mean diameter(μm)	84.97
Shape factor	0.9
Spread parameter	3.78

$$\phi_s = \frac{S_v}{S_p} \tag{1}$$

where S_p is the actual surface area of the particle, S_v is the surface area of a sphere with the same volume as the particle.

Rosin-Rammler method is employed to fit the size distribution of powder particles. In this method, the relationship between the mass fraction of particles and the diameter can be describe as follows:

$$Y_d = e^{-(d/\bar{d})^n} \tag{2}$$

where d is the diameter of the particle, $\bar{d}$ is the mean diameter of the particle, Y_d is the cumulative mass fraction of material with the diameter less than size d. n is the spread parameter describing the uniformity of the diameter distribution of the particles.

3. Mathematical model

Physical and mathematical descriptions of the particle transportation in LDED process include two main aspects: gas jet from single-layer to multi-layer and particle behavior from inside to outside of the CCPFN. The main assumptions in this study are as followed:

(1) The powder-gas flow is regarded as a viscous, incompressible, and steady-state turbulent flow;
(2) The effect of laser beam on gas flow and powder flow is ignored;
(3) Only the gravity, buoyancy and drag force of powder particles are considered;
(4) The size of particles is assumed to follow the general Rossin-Rammler distribution.

3.1. Gas jet flow

In LDED, the flow state of gas jet is turbulent. The numerical simulation of a turbulent flow involves the modification of the Navier-Stokes equations using a time-averaging procedure [16]. For a turbulent flow being steady, incompressible, isothermal, chemically homogeneous, and without body forces, the governing equations for gas jet flow are written as [26]:

Conservation of mass:

$$\frac{\partial(\rho u_j)}{\partial x_j} = 0 \tag{3}$$

where ρ is the gas density, x_j and u_j represent the position and gas velocity component.

Conservation of momentum:

$$\frac{\partial(\rho u_i u_j)}{\partial x_j} = -\frac{\partial p}{\partial x_i} + \frac{\partial \tau_{ij}}{\partial x_j} + \rho g_i + S_i \tag{4}$$

where g_i is the gravitational acceleration, the subscripts $i, j = 1, 2, 3$ are tensor representation, S_i is the source term representing the force applied by the powder, τ_{ij} is the viscous stress given by

$$\tau_{ij} = \left[(\mu+\mu_t)\left(\frac{\partial u_i}{\partial x_j}+\frac{\partial u_j}{\partial x_i}\right)\right]-\frac{2}{3}\mu_t\frac{\partial u_i}{\partial x_i}\delta_{ij} \tag{5}$$

where μ is the molecular viscosity. When $i=j$, $\delta_{ij}=1$, otherwise, $\delta_{ij}=0$, μ_t is the turbulent viscosity expressed as:

$$\mu_t = \rho C_\mu \frac{k^2}{\varepsilon} \tag{6}$$

where k is the turbulent kinetic energy, ε is the dissipation rate of turbulent kinetic energy.

The standard k-ε model here is used [26].

Conservation of kinetic energy of turbulence:

$$\frac{\partial(\rho u_j k)}{\partial x_j} = \frac{\partial}{\partial x_j}\left(\frac{\mu_t}{\sigma_k}\frac{\partial k}{\partial x_j}\right)+G_k+G_b-\rho\varepsilon \tag{7}$$

Conservation of dissipation of kinetic energy of turbulence:

$$\frac{\partial(\rho u_j \varepsilon)}{\partial x_j} = \frac{\partial}{\partial x_j}\left(\frac{\mu_t}{\sigma_\varepsilon}\frac{\partial \varepsilon}{\partial x_j}\right)+C_1\frac{\varepsilon}{k}(G_k+G_b)-C_2\rho\frac{\varepsilon^2}{k} \tag{8}$$

$$G_k = \mu_t\left(\frac{\partial u_i}{\partial x_j}+\frac{\partial u_j}{\partial x_i}\right)\frac{\partial u_i}{\partial x_j} \tag{9}$$

$$G_b = -g_i\frac{\mu_t}{\rho \mathrm{Pr}_t}\frac{\partial \rho}{\partial x_i} \tag{10}$$

$$\mathrm{Pr}_t = \frac{\mu_t C_p}{k_t} \tag{11}$$

where G_k represents the generation of turbulence kinetic energy due to mean velocity gradients, G_b is the generation of turbulence kinetic energy due to buoyancy, Pr_t is Prandtl Number, $C_\mu = 0.9$, $C_1 = 1.44$, $C_2 = 1.92$, $\sigma_\varepsilon = 1.3$ and $\sigma_k = 1.0$ are empirical constants [16].

3.2. Discrete-phase particles

For discrete-phase particles, the moving trajectories model is described based on Euler-Lagrange method, and the trajectory of powder particles is solved by integrating the force balance equation in Lagrange reference frame.

The force balance equation is written as:

$$\frac{du_{pi}}{dt} = F_D(u_i-u_{pi})+\frac{g_i(\rho_p-\rho)}{\rho_p}+F_i \tag{12}$$

where u_{pi} is the particle velocity, u_i is the gas phase velocity, ρ_p is the particle density, F_i is an additional acceleration term and $F_D(u_i - u_{pi})$ is the drag force per unit particle mass given as follows:

$$F_D = \frac{18\mu}{\rho_p {d_p}^2}\frac{C_D \mathrm{Re}}{24} \tag{13}$$

where d_p is the particle diameter, Re is relative Reynolds number defined as follows:

$$\mathrm{Re} = \frac{\rho d_p |u_{pi}-u_i|}{\mu} \tag{14}$$

where C_D is the drag coefficient expressed as [27]:

$$C_D = \frac{24}{\mathrm{Re}}(1+a_1\,\mathrm{Re}^{a_2})+\frac{a_3\,\mathrm{Re}}{a_4+\mathrm{Re}} \tag{15}$$

where

$$\begin{aligned} a_1 &= \exp\left(2.3288-6.4581\phi_s+2.4486{\phi_s}^2\right)\\ a_2 &= 0.0964+0.5565\phi_s\\ a_3 &= \exp\left(4.905-13.8944\phi_s+18.4222{\phi_s}^2-10.2599{\phi_s}^3\right)\\ a_4 &= \exp\left(1.4681+12.2584\phi_s-20.7322{\phi_s}^2+15.8855{\phi_s}^3\right) \end{aligned} \tag{16}$$

Based on the above, the model for the discrete-phase particles is established.

3.3. Computational domain and boundary conditions

Numerical calculation is conducted to quantitatively analyze powder behavior, such as powder velocity, concentration distribution and trajectory in pneumatic transportation process. As shown in Fig. 4, the structure of the CCPFN in region A is meshed with unstructured tetrahedral and hexahedral elements and the structure in region B is meshed with structured hexahedral elements. As a result, the total grid number is about 4,200,000. The gas inlets of ISGF, OSGF and CGF are set as velocity inlet, which can be calculated based on the gas flow rate in Table 3 and Table 4. The outlet of the computational domain is considered as pressure outlet with the pressure of 0 MPa. In order to ensure the precision of the calculation, the convergence accuracy is set to be 10^{-5}.

3.4. Inelastic collision between particle and nozzle wall

In LDED process, the collision between the particles and the nozzle wall is an inelastic dynamic process, as the process is affected by impact velocity, size and shape of powders, and the materials of particles and wall. The momentum loss caused by inelastic collision of particle-wall is expressed by restitution coefficient:

$$e = \frac{V_r}{V_i} \tag{17}$$

where e is the restitution coefficient, V_r is the rebound velocity of particles, V_i is the incident velocity of particles. When e is 1, it means that the collision between particles and wall is elastic and there is no

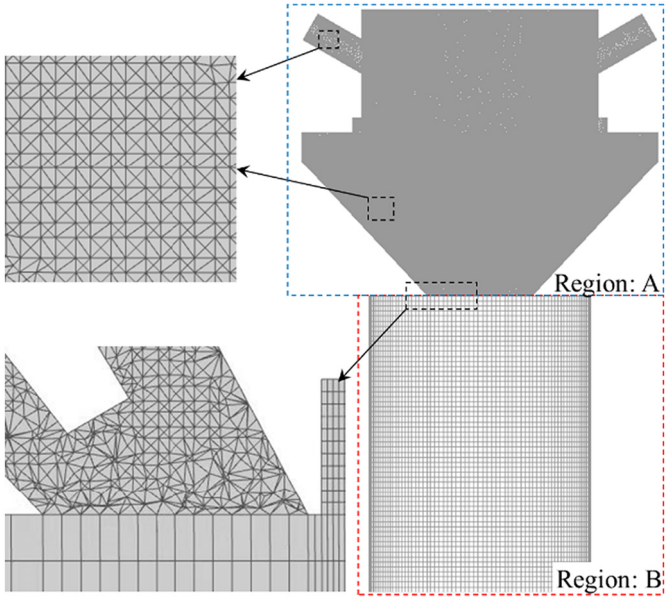

Fig. 4. Grid distribution of calculation area.

momentum loss of the particles. When the collision is inelastic, e is less than 1.

4. Results and discussion

4.1. Exit morphology and velocity of particles

The exit morphology and outlet velocity of particles just ejected from the CCPFN, which is determined by the mutual effect of single-layer jet and inelastic collision between particles and wall, are important features of powder transport behavior. The exit morphology of particles is shown in Fig. 5. To obtain the exit velocity of the particles and the focusing properties of the powder flow (such as focus position and focus length), the powder flow image must be preprocessed by image processing techniques. In this paper, in order to reduce the influence of random movements of the particles in the gas flow, a normalized image processing method is used to obtain the superposition of gray-scale from 400 consecutive images of exit morphology, as shown in Fig. 5 (b). The coordinate of powder focus can be accurately positioned from the superimposed gray image. When the annular powder flow is emitted obliquely, the particles focus at a position about 8 mm directly below the CCPFN outlet.

Particle tracking using PIVlab tool [28] is employed to obtain detailed characteristics of dispersion behavior of particles at the outlet, providing in-depth measurement and physical explanations of particle velocity dispersion on different transportation processes.

As shown in Fig. 5, the particles in the region with the width of 18 mm and the length of 10 mm are used for statistical evaluation of outlet velocity. As shown in Fig. 6, when the CGF rate is 4 L/min, the outlet velocity of particles ranges from 0.4 m/s to 0.92 m/s. Quantitative experimental analysis can provide practical guidance for theoretical and simulation research.

In this study, the experimental outlet velocity distribution obtained by particle tracking is employed to inversely calculate the restitution coefficient using trial-and-matching method. In this method, the restitution coefficients of 0.95, 0.9, 0.85 and 0.8 are used to calculate the outlet velocity of particles base on the CFD- DPM two-way coupling

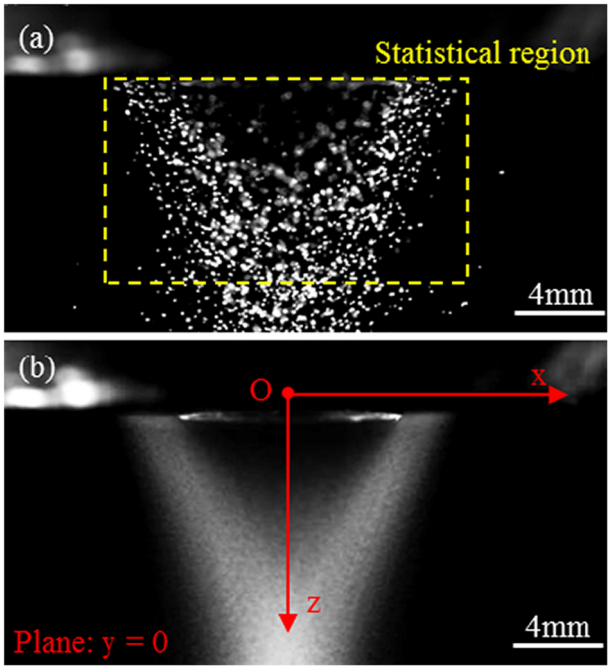

Fig. 5. Exit morphology of particles (a) The original image (b) Grayscale image after superposition.

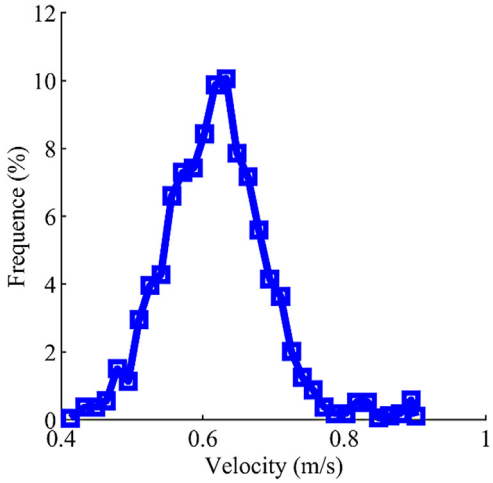

Fig. 6. Outlet velocity of particles at the OSGF rate of 4 L/min.

model established in Section 3.2, and the calculated outlet velocity of particles is shown in Fig. 7. It is assumed that the inlet velocity of the particle is equal to the velocity of the CGF. Obviously, when the restitution coefficient is 0.9, the outlet velocity distribution obtained by numerical calculation is ranged from 0.4 m/s to 0.9 m/s and the statistical velocity distribution is consistent with the experimental result by particle tracking method. Thus the restitution coefficient of 0.9 is determined to describe the loss of particle velocity in inelastic collision. In this way, the uncertain inelastic collision behavior between particles and the wall is expressed by a determined restitution coefficient.

In order to visualize the transportation process of particles after being injected from the nozzle, image processing technique is used to analyze the transportation trajectories, velocity and concentration of the selected particles. Firstly, the transportation morphologies of five moments with the interval of three frames are employed and the original morphologies are shown in Fig. 8(a). Secondly, the threshold selection method [29] is used to process the powder flow image and the binary morphologies are displayed in Fig. 8(b). The white dots in Fig. 8 (a) and Fig. 8(b) represent the transport positions of the particles. Thirdly, the transport positions of the particles at different moments are marked in color, as shown in Fig. 8(c). Finally, the colored morphologies of the particles at different moments are superimposed into one image (shown as Fig. 8(d)). Therefore, the superimposed image can be used to track the transportation trajectory and velocity of the particles. As shown in Fig. 8(e), four particles are selected to visualize the transportation process. The length of the white lines in Fig. 8(e) can be used to quantitatively calculate the transportation velocities of particles and the velocities of particleI, II, III and IV are 0.55 m/s, 0.43 m/s, 0.61 m/s, 0.53 m/s, respectively. The velocities and directions of the particles in transportation process are almost unchanged. The transportation direction of particlesIand IVis almost parallel to the gravity direction, and there is no convergence trend, resulting in the decrease of mass concentration of particles at the focus position. The transportation direction of particles II and III is about 20° from the z direction and points to the convergence center, which is conducive to the convergence of particles at the focus position.

4.2. Mass concentration distribution

In this paper, optical diagnosis combined with image processing technology is used to semi-quantitatively study the spatial concentration distribution of powder. Fig. 9 shows the transport morphology of powder jet under different OSGF. The gray level in particle transport morphology describes the powder mass, which can be used for the semi-qualitative analysis of the powder concentration and focus

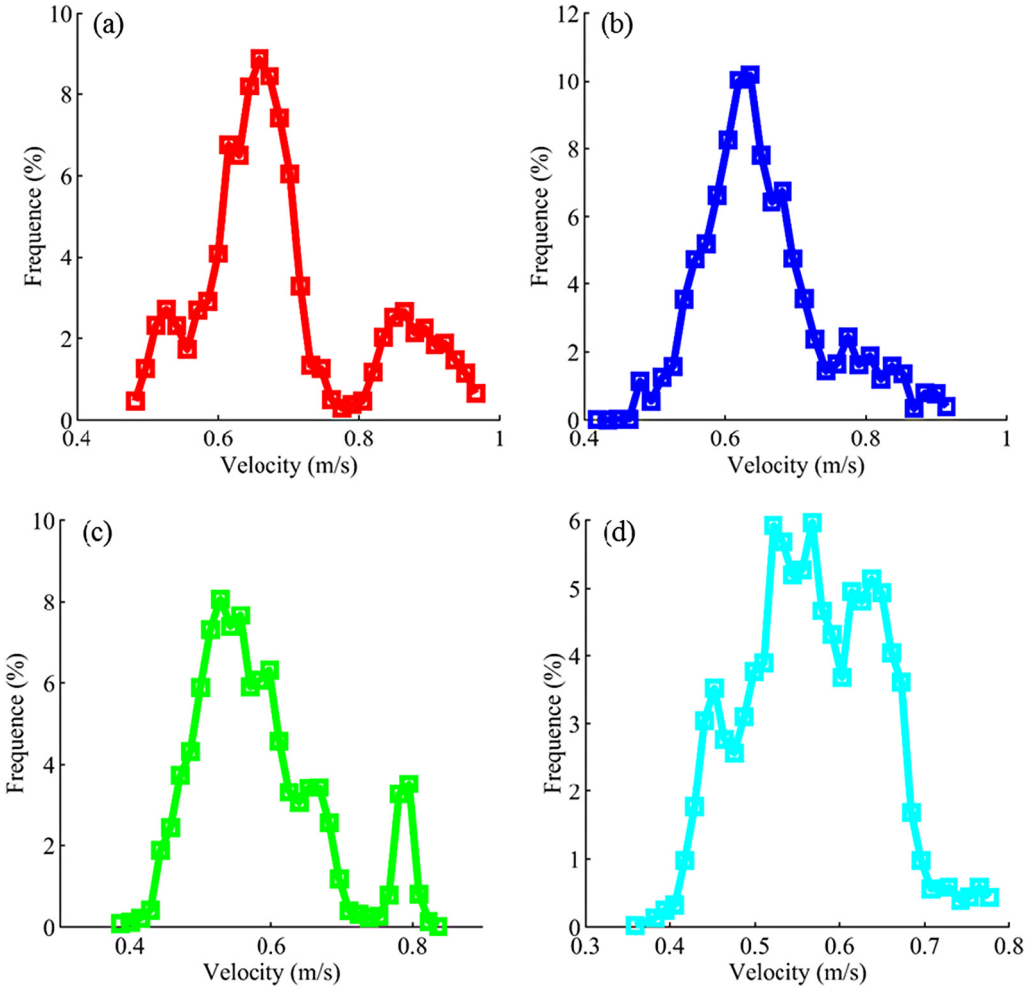

Fig. 7. Numerical outlet velocity of particles with the restitution coefficient of (a) 0.95 (b) 0.9 (c) 0.85 (d) 0.8.

characteristics (such as focus position and focus length). When the OSGF rate is small, a large number of particles escape from the focus trajectory. With the increase of the OSGF rate, the number of escape particles decreases gradually. When the flow is 20 L/min, the focus characteristic of powder for CCPFN is the best, with the fewest escape particles and smallest focus radius. Under this powder feeding process, the focus length is about 13 mm. When the OSGF rate is 30 L/min, most particles can move on the focusing track before focusing, and there are almost no dispersed particles. However, after focusing, most particles diverges in an umbrella shape. This is because that the effect of the extra drag force exerted by the excessive OSGF on the particles is greater than the combined effect of other jet flows and particle gravity. After focusing, the particles continue to move along the direction of the drag force exerted by the OSGF.

The semi-quantitative analysis of powder concentration at the OSGF rate of 20 L/min is shown in Fig. 10. The grayscale image in Fig. 10(a) is the spatial concentration distribution by superimposing 400 consecutive pictures taken by optical diagnostic system. The variation of the relative gray level with the transverse direction at the positions of 6 mm ($z = 6$ mm), 14 mm($z = 14$ mm), 22 mm($z = 22$ mm) under the CCPFN outlet is shown in Fig. 10(b). At the position of $z = 6$ mm, there is a bimodal distribution for the grayscale curve. At the center of the powder flow, the gray level is much lower than the peak gray level. At the positions of $z = 14$ mm and $z = 22$ mm, the gray value can be described as Gaussian distribution, and the central axis of the curve coincides with the central position of the powder flow. It is worth noting that the peak gray level of $z = 14$ mm is slightly higher than that of $z = 22$ mm, which means that the particles gradually focus from position of $z = 6$ mm to $z = 14$ mm, and diverge from position of $z = 14$ mm to $z = 22$ mm.

Spatial concentration distribution of powder particles under different OSGF rate is calculated quantitatively and shown in Fig. 11. The restitution coefficient of 0.9 determined by trial-and-matching method is used to measure the inelastic collision behavior of particles and the inner wall of the CCPFN. The simulated mass concentration for the same position and process parameters used in Fig. 10 is shown in Fig. 12. By comparing the numerical mass concentration (shown in Fig. 12) and that obtained semi-quantitatively by optical diagnosis method (shown in Fig. 10), it is found that at the position of $z = 6$, there is a bimodal mass concentrate distribution for the two method. At the position of $z = 14$ and $z = 22$, mass concentration distributions of particles are consistent and approximately obey by the Gaussian function. In addition, it should be noted that at the position of $z = 6$, there is difference between the experimental and calculated mass concentration at the center position. This is because that the cylindrical auxiliary light source is used in the experiment, and the particles in the focus range of the high speed camera are photographed, which causes the powder concentration higher than that from calculation. Consistency of spatial concentration distribution further proves the correctness of using the restitution coefficient of 0.9 to characterize the inelastic collision behavior between the particle and the wall. The consistency between the experimental and calculated mass concentration

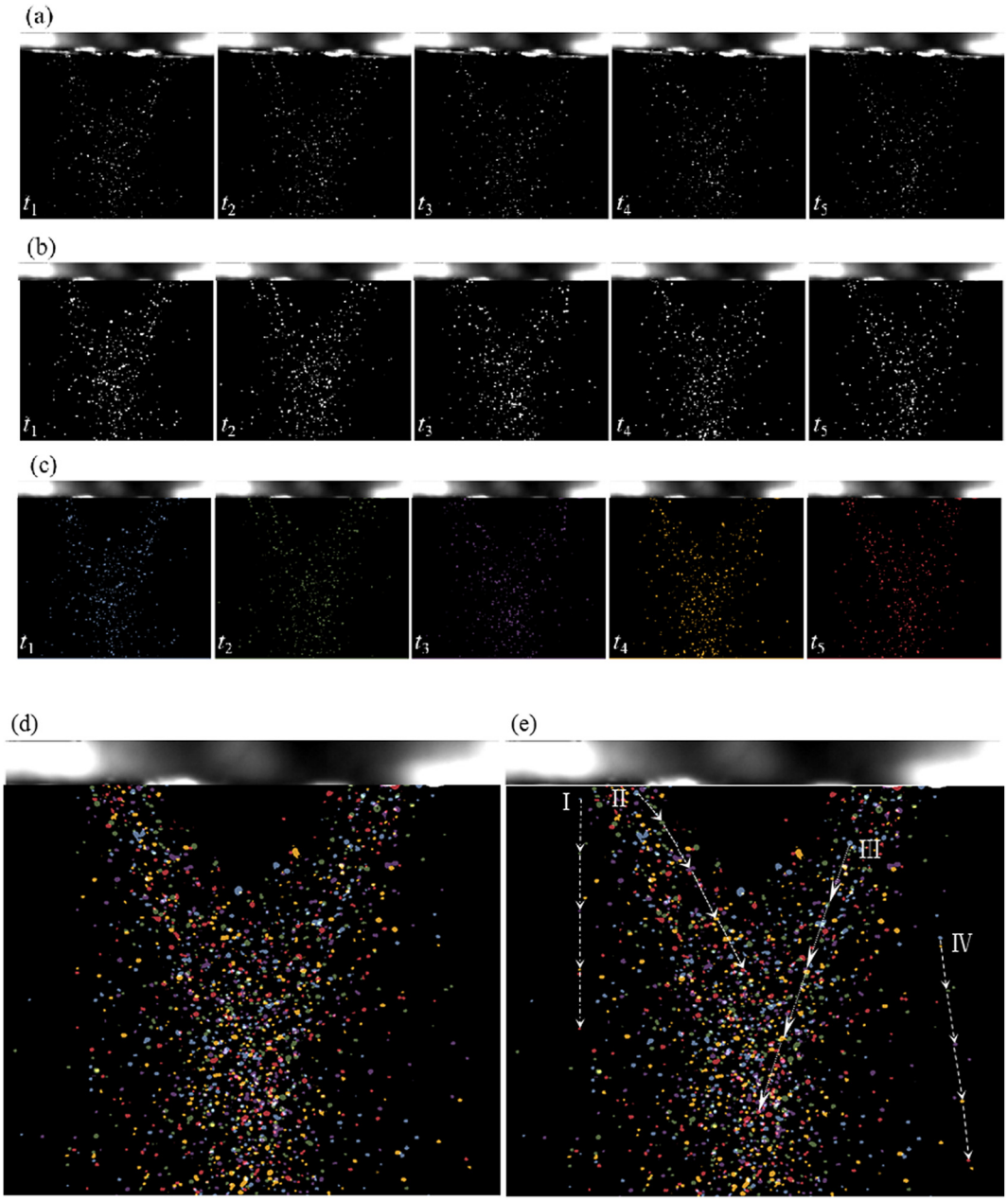

Fig. 8. Pneumatic transmission process of particles (a) Original morphologies (b) Binary morphologies (c) Colored morphologies (d) Superimposed morphology (e) Particles transmission tracking.

provides a basis for the approximate simplification of the inelastic collision behavior between particles and wall.

The spatial concentration distribution of powders can be intuitively and quantitatively obtained through the cloud map of concentration field. The cloud map of concentration field under different OSGF is shown in Fig. 11. When the OSGF changes, the initial position of the powder focus is almost unchanged, but the concentration distribution below the focus position is greatly affected by the OSGF. When the OSGF is less than 15 L/min, there is a focused powder distribution with the length of approximately 3.5 mm(length of l_2 shown as Fig. 11(c)) at the position of z = 8 mm(shown as the line l_1 in Fig. 11(c)), and the mass concentration of particles reaches 15 kg/m^3. When the OSGF is 20 L/min, the powder concentration field is obviously narrowed, but the focus length reaches 13.5 mm (shown as the position of the line l in Fig. 11(e)).

Quantitative analysis of powder concentration field provides a prerequisite for controlling the forming shape and improving the dimensional accuracy. The OSGF can be used to control the powder concentration distribution, so that the concentration distribution of particles can meet the process requirement for part repairing, functional coating cladding and additive manufacturing.

4.3. Numerical analysis of the gas jet flow

The velocity field distribution of CGF, which is determined by the channel structure of the CCPFN, is an important determinant of the powder transport in single-layer jet. When three channels of gas flow is emitted from the CCPFN, it interacts in space to determine the transportation behavior of powders in multi-layer jet. Fig. 13 represents the partial views of fluid velocity field in the CGF channel. The structure of

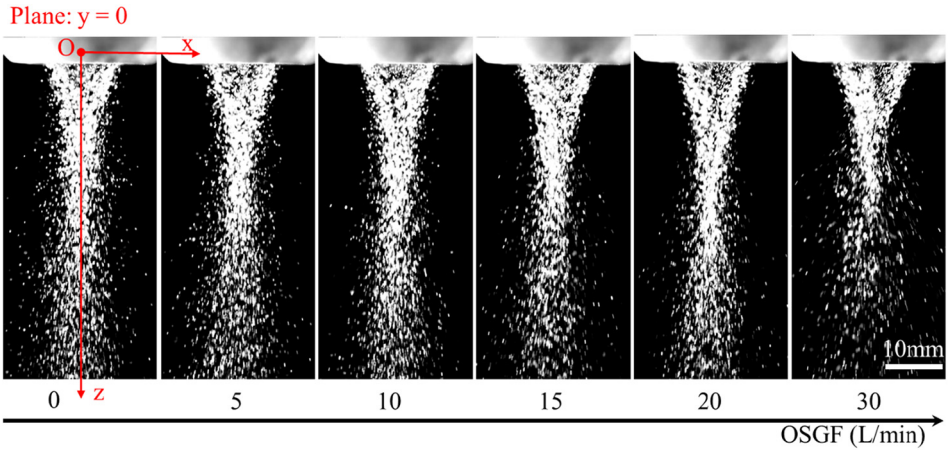

Fig. 9. Transport morphology of powder jet under different OSGF rate.

CGF channel consists of three parts. First, the gas is injected to the channel through four inlets with the direction of 30° from horizontal plane (as shown in Fig. 1(c) from point A(p_A) to p_B). In the second stage, CGF flows into the vertical downward annular channel (as shown in Fig. 1(c) from p_B to p_C), of which the clearance is a constant. And then, it enters the convergence interval with the angle of 30° to the horizontal plane(as shown in Fig. 1(c) from p_C to p_D). As can be seen from Fig. 13, in the internal flow field of CCPFN, the outlet velocity and inlet velocity of the CGF are relatively high. The quantitative results of CGF velocity are of great value to study the influence of drag force on powder transport characteristics. Fig. 14 quantitatively shows the variation of CGF velocity along the direction of p_A → p_B → p_C → p_D (as shown in Fig. 13). The incident velocity of the CGF is approximately calculated by $v = Q/4S$, where Q is the CGF rate and S is the cross-sectional area of powder inlet. When CGF rate is 4 L/min, the injection velocity is about 1.33 m/s. After slight acceleration, the flow velocity drops sharply to about 0.3 m/s. This is caused by the CCPFN structure of vertical downward annular channel. The cross-sectional area of CGF channel suddenly increases, resulting in a sharp decrease in flow velocity. The CGF gradually accelerates after flowing into the wedge gap, and when reaching the outlet, the gas velocity is close to the velocity at the inlet. It can be clearly seen from Fig. 15 that the CGF velocity at the outlet is uniform in the circumferential direction of the outlet.

It can be seen from Eq. (12) that the acceleration of particles is mainly determined by the difference between CGF velocity and particle velocity. In the process of pneumatic transportation of particles, the gas jet flow is steady. Therefore, when the velocity field of the CGF is obtained, the process of particle transportation by gas flow field can be fixed and solved.

When the ISGF is obliquely emitted, a multi-layer jet is formed between the CCPFN outlet and the substrate. Characteristics of multi-layer jet under different OSGF are studied in this paper. Fig. 16 describes the velocity field and streamlines of multi-layer jet flow under different OSGF at the ISGF rate of 10 L/min, the CGF rate of 4 L/min, and the powder feeding rate of 30 g/min. The white streamlines represent the direction of jet flow. The effect of OSGF on multi-layer jet from p_E to p_F (as shown in Fig. 1(c)) is studied quantitatively and shown in Fig. 17. The influence of OSGF rate on gas jet flow includes two aspects: one is the influence on the surrounding air flow, and the other is the effect on multi-layer jet zone located in the central flow field. With the increase of the OSGF rate, there is a pattern transformation of vortex for surrounding air. Toroidal vortex of the surrounding air is formed under the OSGF of 10 L/min. When the OSGF rate is greater than 15 L/min, an outward vortex can be formed at the periphery of the central flow field, which ensures the isolation of air during powder transportation. When the OSGF is 30 L/min, the surrounding air flow forms a small inward vortex at the jet outlet. Between the center of the multi-layer jet flow and outward vortex is the diffusion zone, in which the gas jet flow diffuses and the flow velocity drops in gradient. In the central jet flow zone, under the influence of different OSGF rate, the gas flow remains a vertical downward transportation. At the distance of 8 mm from the CCPFN outlet, the velocity of multi-layer jet reaches the

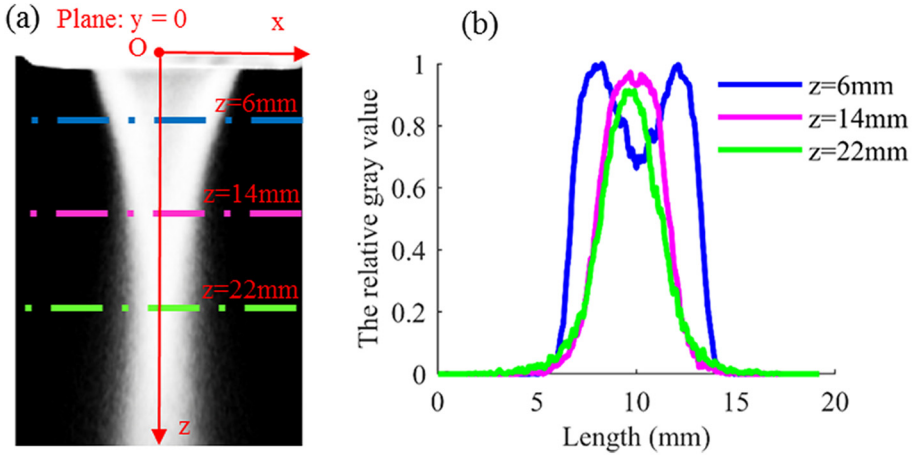

Fig. 10. Spatial concentration distribution described by (a)The gray scales of powder morphology (b) Gray scales distribution as a function of lateral position.

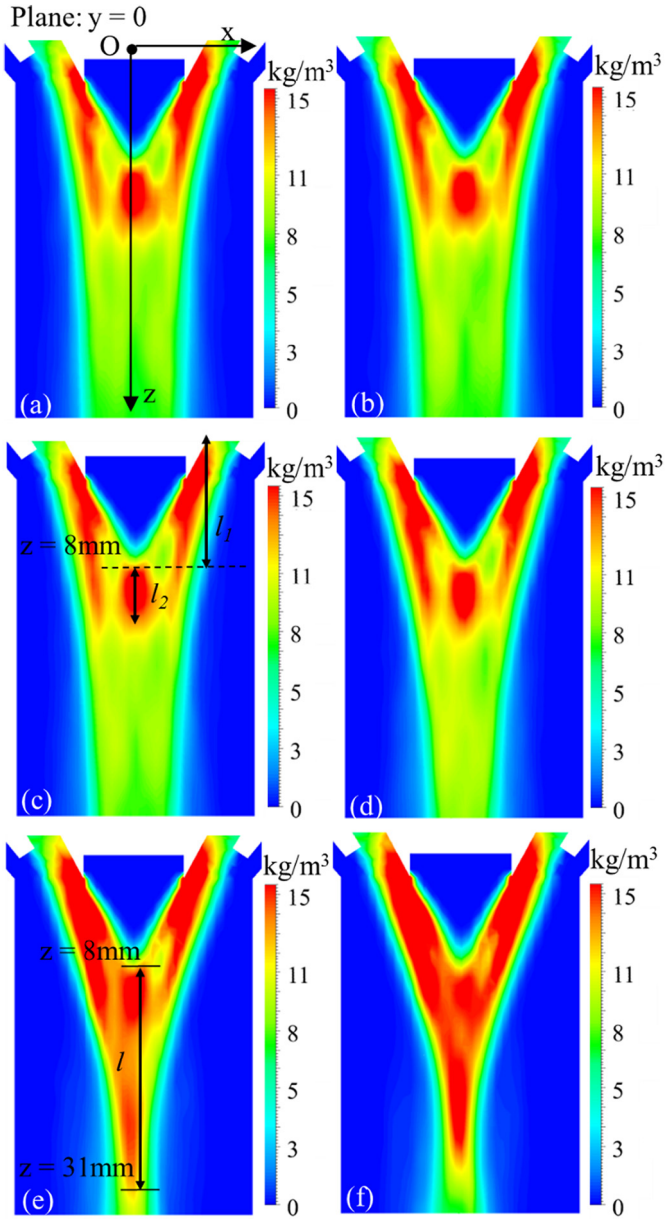

Fig. 11. Simulated mass concentration with the OSGF rate of (a) 0 L/min (b) 5 L/min (c) 10 L/min (d) 15 L/min (e) 20 L/min (f) 30 L/min.

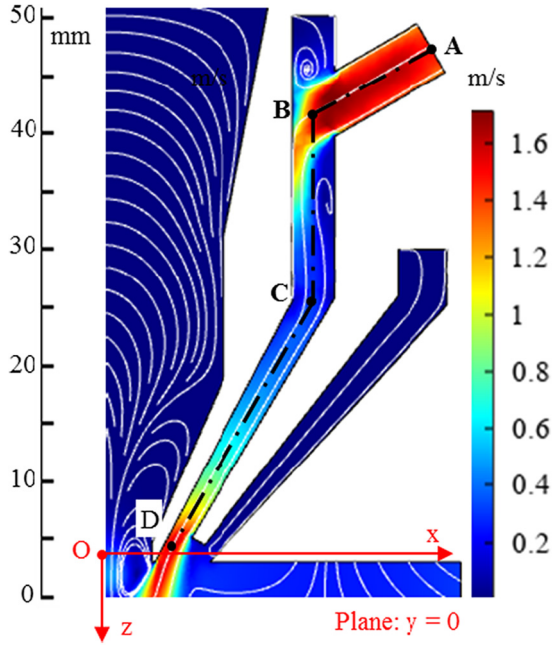

Fig. 13. Gas velocity field and streamline diagram for CGF channel.

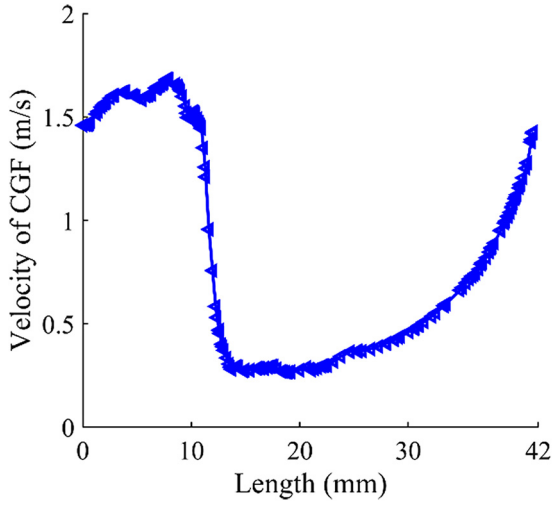

Fig. 14. Velocity of CGF along channel direction.

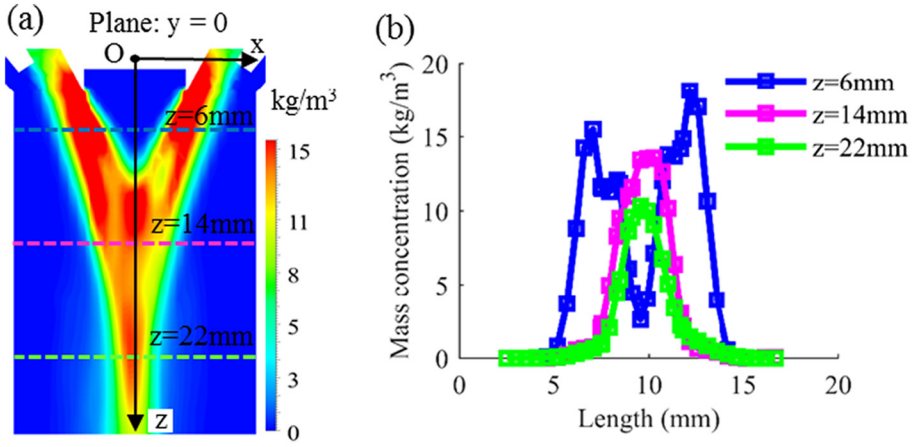

Fig. 12. Simulated mass concentration with the OSGF rate of 20 L/min (a) Simulated mass concentration field (b) Mass concentration as a function of lateral position.

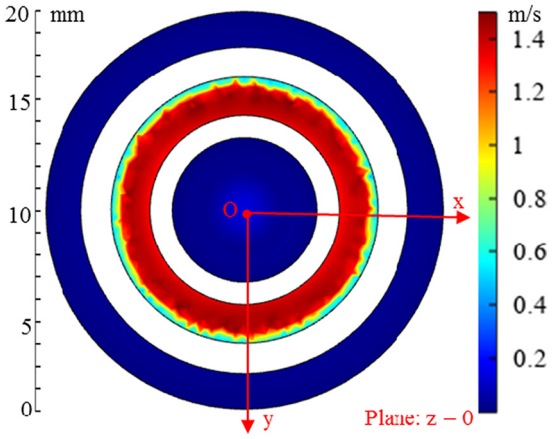

Fig. 15. Velocity field of CGF in outlet section.

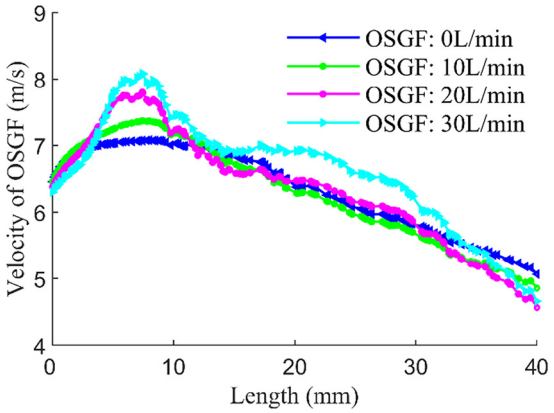

Fig. 17. Velocity of OGGF along channel direction under different flow rate.

maximum. With the increase of OSGF rate, the maximum multi-layer jet velocity gradually increases, which may play a positive role in improving the convergence characteristics of the powder.

Noteworthy, there are no reliable data about the relationship between dynamic transportation characteristic of powders and the detailed structure of the CCPFN from single-layer to multi-layer jet flow. It is of great value to study the gas jet transportation process from single-layer to multi-layer jet, which provides theoretical guidance for explaining the particle transport mechanism and the optimal design of CCPFN.

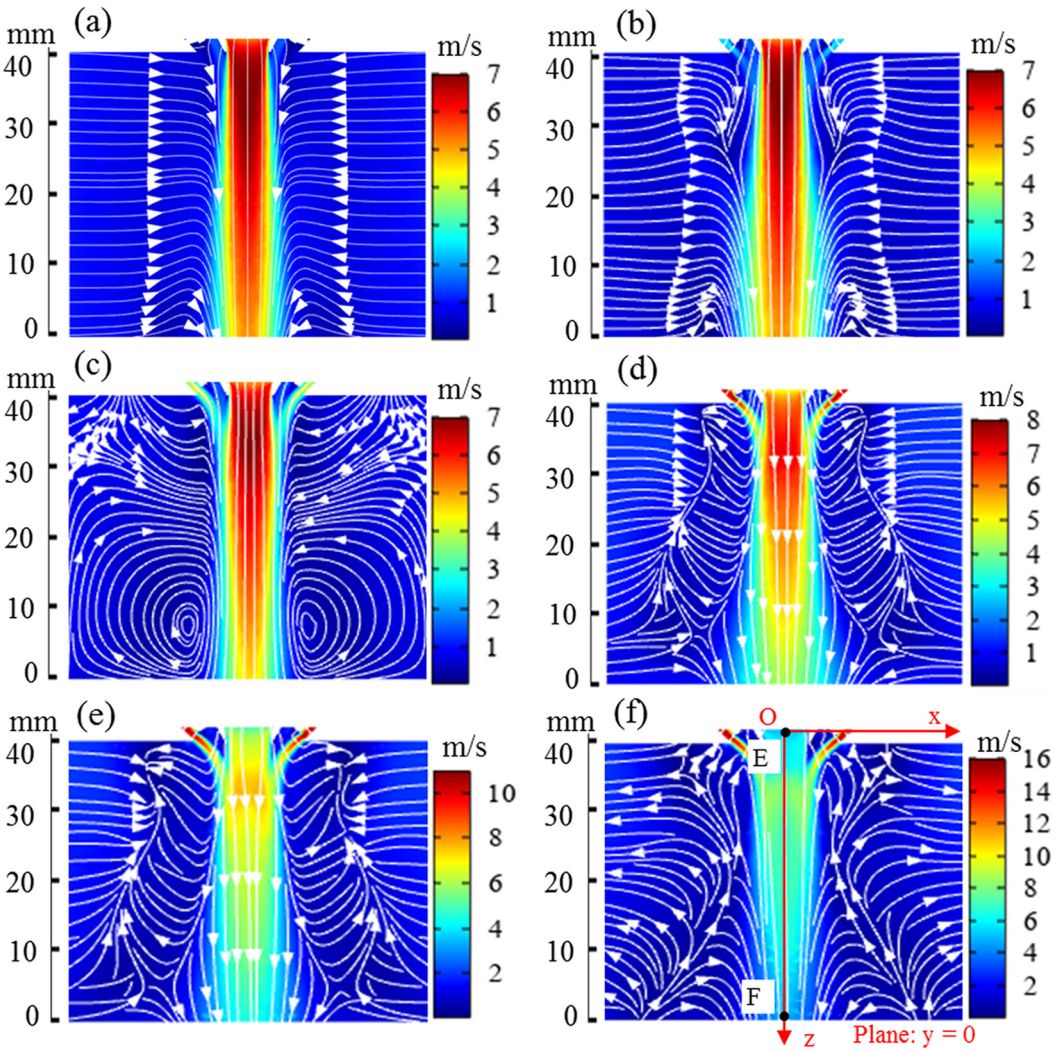

Fig. 16. Velocity field and streamline diagram in longitudinal section under the OSGF rate of (a) 0 L/min (b) 5 L/min (c) 10 L/min (d) 15 L/min (e) 20 L/min (f) 30 L/min.

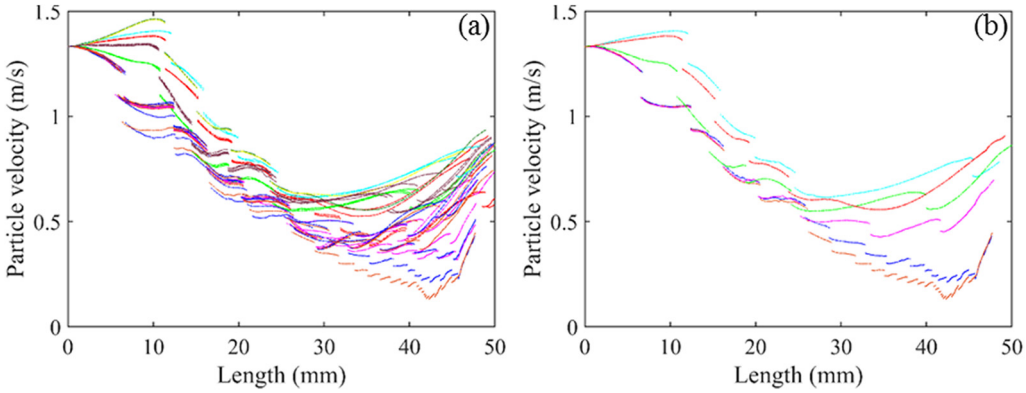

Fig. 18. Variation of particle velocity along the motion trajectories (a) Trajectories of thirty particles (b) Trajectories of six particles.

4.4. Particle trajectory in the inner CCPFN

Although the transportation process can be intuitively studied through the experimental research combined with image processing method, neither the visualization of particles colliding with the wall, nor the explanation of particle transportation mechanism in the inner CCPFN can be realized directly from experiments. In this paper, based on Euler-Lagrange theory, the velocity variation of the particles along the motion trajectories in the inner CCPFN at the CGF rate of 4 L/min and the powder feeding rate of 30 g/min, is calculated and the trajectories of thirty particles, whose velocity almost covers the whole range of exit velocity, are shown in Fig. 18 (a). In order to clearly display the particle velocity history along the trajectory, six characteristic trajectories of particles are selected and shown in Fig. 18 (b). Along the particle trajectory, the particle velocity distribution gradually diverges, which is due to the different degree of inelastic collision between the particle and the inner wall of the CCPFN, and the effect of drag force of the CGF.

Before the first collision, there are three kinds of velocity variation for particles, namely, acceleration, constant velocity and deceleration. The reason is that the particles are subjected to different drag force, which is caused by different entrance position and independent cylindrical entrance structure (as shown in Fig. 1(c) from p_A to p_B). After the first collision, the particles enter a vertical downward circular channel (as shown in Fig. 1(c) from p_B to p_C), and the velocity of all particles decreases until the flight distance reaches about 20 mm. This is due to the decrease of CGF velocity causing the reduction of drag force and the inelastic collision between the particles and the wall causing the kinetic energy loss of the particles. When the flight distance is about 20 mm to 30 mm, the particles enter the convergence channel (as shown in Fig. 1(c) from p_C to p_D), the velocity of the CGF increases, and the deceleration process of the particles slows down. At this time, the drag force of CGF increases, but it is not enough to offset the kinetic energy loss caused by inelastic collision. When the flight distance of the particles reaches 30 mm, the drag force gradually plays a major role in the movement of the particles, and the particles begin to accelerate until they are emitted from the CCPFN. It is worth noting that when the flight trajectory is over 30 mm, the motion of some particles deviates greatly from the streamline direction of the gas field. This is because of the increase of collision frequency between the particles and the wall caused by the reduction of the wedge-shape clearance, intensifying the outlet velocity dispersion of particles and fluctuation of particle trajectory, which results from coupling effects of drag force and inelastic collision. Moreover, the structure of CCPFN determines the velocity field distribution of CGF and affects the degree and frequency of particle collision with the inner wall of CCPFN.

Numerical simulation method gives a quantitative analysis of the influence factors of pneumatic transportation of particles in LDED process and fully proves the exit behavior of the particles from the perspective of mechanism. The relationship between the particle transport process and the structure of CCPFN is clarified, which provides theoretical guidance for optimizing the structure design of CCPFN. It is advised to shorten the structure of CCPFN, inside which the velocity of the particles decreases. This is conducive to reducing the outlet velocity fluctuation of particles and making the velocity distribution more uniform.

5. Conclusion

This paper investigated the powder flow distribution of CCPF in the LDED using numerical analysis and experimental investigation. The concentration distribution of powders and velocity field of gas at different OSGF were obtained. Based on Euler-Lagrange theory, the velocity variation of the particles along the motion trajectories has been calculated and the particle transportation mechanism has been deeply explained.The following conclusions can be drawn from the study:

(1) A trial-and-matching method has been developed to determine the restitution coefficient, which can be used to describe the inelastic collision behavior between the particle and the wall. The restitution coefficient was determined to be 0.9, which is verified from two aspects. One is that the simulated outlet velocity distribution of particles is consistent with that obtained from particle tracking method. The other is that the spatial concentration distribution of powders obtained through optical diagnosis method is correspondent with simulated concentration distribution.

(2) With the increase of the OSGF rate, there is a pattern transformation of vortex for surrounding air. When the flow is 20 L/min, the focus characteristic of powders for CCPFN is the best, with the fewest escape particles, smallest focus radius and focus length of 13 mm.

(3) The velocity distribution of CGF in the inner CCPFN and the restitution coefficient are the two mutually coupled factors that determine the outlet velocity of particles. Frequent inelastic collisions and the decrease of the CGF velocity lead to velocity dispersion and trajectory fluctuation of particles. When the inlet velocity of particles is 1.33 m/s, the outlet velocity ranged from 0.4 m/s to 0.9 m/s.

(4) It is conducive to reducing the outlet velocity fluctuation of particles and making the outlet velocity distribution more uniform by shortening the structure of the vertical downward annular channel and the convergence interval of the CCPFN.

Funding

This work was supported by the National Natural Science Foundation of China (Nos. 11502269 and 11672304), and plan of Beijing Municipal Commission of Science and Technology (No. Z181100003818015).

Availability of data and material

The authors confirm that the data supporting the findings of this study are available within the article. The raw data that support the findings of this study are available from the corresponding author, upon a reasonable request.

Code availability

Not applicable.

Ethics approval

The research does not involve human participants or animals, and the authors warrant that the paper fulfills the ethical standards of the journal.

Consent to participate

It is confirmed that all the authors are aware and satisfied of the authorship order and correspondence of the paper.

Consent for publication

The manuscript is approved by all authors for publication; all the authors listed have approved the manuscript that is enclosed.

CRediT authorship contribution statement

Yanhua Bian: Investigation, Methodology, Validation, Writing – original draft. **Xiuli He:** Supervision, Project administration, Conceptualization, Writing – review & editing. **Gang Yu:** Resources, Supervision, Funding acquisition, Data curation, Writing – review & editing. **Shaoxia Li:** Funding acquisition, Data curation, Investigation, Software. **Chongxin Tian:** Visualization, Investigation, Validation, Software. **Zhiyong Li:** Investigation, Data curation, Validation. **Yanmei Zhang:** Data curation, Formal analysis, Software. **Junming Liu:** Investigation, Data curation, Visualization.

Declaration of Competing Interest

The authors declare no competing interests.

References

[1] D. Zhang, R. Yu, K. Chen, X. Yang, Y. Liu, Y. Yin, Corrosion and corrosion-friction properties of plasma cladding wear-resistant layer on fe-based alloy, Mater. Res. Express. 5 (2) (2018) 026525, https://doi.org/10.1088/2053-1591/aaae7f.

[2] T. Tarasova, G. Gvozdeva, R. Ableyeva, Aluminium matrix composites produced by laser based additive manufacturing, Mater. Today: Proc. 11 (2019) 305–310, https://doi.org/10.1016/j.matpr.2018.12.149.

[3] B. Onuike, B. Heer, A. Bandyopadhyay, Additive manufacturing of Inconel 718-copper alloy bimetallic structure using laser engineered net shaping (LENS (TM)), Addit. Manuf. 21 (2018) 133–140, https://doi.org/10.1016/j.addma.2018.02.007.

[4] Z. Liu, Q. Jiang, T. Li, S. Dong, S. Yan, H. Zhang, B. Xu, Environmental benefits of remanufacturing: a case study of cylinder heads remanufactured through laser cladding, J. Clean. Prod. 133 (2016) 1027–1033, https://doi.org/10.1016/j.jclepro.2016.06.049.

[5] A. Khajepour, E. Toyserkani, S. Corbin, Laser Cladding || Background and Basic Overview, 2004 https://doi.org/10.1201/9781420039177.

[6] J.P. Kruth, M.C. Leu, T. Nakagawa, Progress in additive manufacturing and rapid prototyping, CIRP Ann. 47 (2) (1998) 525–540, https://doi.org/10.1016/S0007-8506(07)63240-5.

[7] J. Gao, C. Wu, X. Liang, Y. Hao, K. Zhao, Numerical simulation and experimental investigation of the influence of process parameters on gas-powder flow in laser metal deposition, Opt. Laser Technol. 125 (1–2) (2019) 106009, https://doi.org/10.1016/j.optlastec.2019.106009.

[8] A.J. Pinkerton, An analytical model of beam attenuation and powder heating during coaxial laser direct metal deposition, J Phys D-Appl Phys. 40 (2007) 7323–7334, https://doi.org/10.1088/0022-3727/40/23/012.

[9] J.M. Lin, Numerical simulation of the focused powder streams in coaxial laser cladding, J. Mater. Process. Technol. 105 (1–2) (2000) 17–23, https://doi.org/10.1016/s0924-0136(00)00584-7.

[10] A. Zhang, D. Li, Z. Zhou, G. Zhu, B. Lu, Numerical simulation of powder flow field on coaxial powder nozzle in laser metal direct manufacturing, Int. J. Adv. Manuf. Technol. 49 (9–12) (2010) 853–859, https://doi.org/10.1007/s00170-010-2657-8.

[11] G. Zhu, D. Li, A. Zhang, Y. Tang, Numerical simulation of metallic powder flow in a coaxial nozzle in laser direct metal deposition, Opt. Laser Technol. 43 (1) (2011) 106–113, https://doi.org/10.1016/j.optlastec.2010.05.012.

[12] I. Tabernero, A. Lamikiz, E. Ukar, L.N. Lopez de Lacalle, C. Angulo, G. Urbikain, Numerical simulation and experimental validation of powder flux distribution in coaxial laser cladding, J. Mater. Process. Technol. 210 (15) (2010) 2125–2134, https://doi.org/10.1016/j.jmatprotec.2010.07.036.

[13] P. Nie, O.A. Ojo, Z. Li, Modeling analysis of laser cladding of a nickel-based superalloy, Surf. Coat. Technol. 258 (2014) 1048–1059, https://doi.org/10.1016/j.surfcoat.2014.07.030.

[14] B. Zhang, C. Coddet, Numerical study on the effect of pressure and nozzle dimension on particle distribution and velocity in laser cladding under vacuum base on CFD, J. Mater. Process. Technol. 23 (2016) 54–60, https://doi.org/10.1016/j.jmapro.2016.05.019.

[15] J. Zhang, L. Yang, W. Zhang, J. Qiu, H. Xiao, Y. Liu, Numerical simulation and experimental study for aerodynamic characteristics and powder transport behavior of novel nozzle, Opt. Laser Eng. 126 (2020) 105873 https://doi.org/10.1016/j.opdaseng.2019.105873.

[16] J. Ibarra-Medina, A.J. Pinkerton, A CFD model of the laser, coaxial powder stream and substrate interaction in laser cladding, Phys. Procedia 5 (2010) 337–346, https://doi.org/10.1016/j.phpro.2010.08.060.

[17] H. Pan, F. Liou, Numerical simulation of metallic powder flow in a coaxial nozzle for the laser aided deposition process, J. Mater. Process. Technol. 168 (2) (2005) 230–244, https://doi.org/10.1016/j.jmatprotec.2004.11.017.

[18] O.B. Kovalev, A.V. Zaitsev, D. Novichenko, I. Smurov, Theoretical and experimental investigation of gas flows, powder transport and heating in coaxial laser direct metal deposition (DMD) process, J. Therm. Spray Technol. 20 (3) (2011) 465–478, https://doi.org/10.1007/s11666-010-9539-3.

[19] O.B. Kovalev, I.O. Kovaleva, I.Y. Smurov, Numerical investigation of gas-disperse jet flows created by coaxial nozzles during the laser direct material deposition, J. Mater. Process. Technol. 249 (2017) 118–127, https://doi.org/10.1016/j.jmatprotec.2017.05.041.

[20] H. Liu, X. He, G. Yu, Z. Wang, S. Li, C. Zheng, W. Ning, Numerical simulation of powder transport behavior in laser cladding with coaxial powder feeding, Sci. China: Phys. Mech. Astron. 58 (10) (2015) 104701, https://doi.org/10.1007/s11433-015-5705-4.

[21] L. Li, Y. Huang, C. Zou, W. Tao, Numerical study on powder stream characteristics of coaxial laser metal deposition nozzle, Crystals 11 (3) (2021) 282, https://doi.org/10.3390/cryst11030282.

[22] T. Hua, F. Zhang, R. Wen, C. Jing, W. Huang, Experiment study of powder flow feed behavior of laser solid forming, Opt. Laser Eng. 50 (3) (2012) 391–398, https://doi.org/10.1016/j.optlaseng.2011.10.017.

[23] N.K. Yu, F.R. Iskhakov, A.I. Shpilev, G.A. Kh, Optical diagnostics and optimization of the gas-powder flow in the nozzles for laser cladding, Opt. Laser Technol. 108 (2018) 310–320, https://doi.org/10.1016/j.optlastec.2018.07.001.

[24] J. Wu, P. Zhao, H. Wei, Q. Lin, Y. Zhang, Development of powder distribution model of discontinuous coaxial powder stream in laser direct metal deposition, Powder Technol. 340 (2018) 449–458, https://doi.org/10.1016/j.powtec.2018.09.032.

[25] D.V. Sergachev, O.B. Kovalev, G.N. Grachev, A.L. Smirnov, P.A. Pinaev, Diagnostics of powder particle parameters under laser radiation in direct material deposition, Opt. Laser Technol. 121 (2020) 105842 https://doi.org/10.1016/j.optlastec.2019.105842.

[26] M.A. Serag-Eldin, D.B. Spalding, Computations of three-dimensional gas turbine combustion chamber, J. Eng. Power. 101 (1979) 327–336, https://doi.org/10.1115/1.3446580.

[27] A. Haider, O. Levenspiel, Drag coefficient and terminal velocity of spherical and non-spherical particles, Powder Technol. 58 (1) (1989) 63–70, https://doi.org/10.1016/0032-5910(89)80008-7.

[28] W. Thielicke, E.J. Stamhuis, PIVlab-towards user-friendly, affordable and accurate digital particle image velocimetry in MATLAB, J. Open Res. Softw. 2 (2014) 1202–1211, https://doi.org/10.5334/jors.bl.

[29] N. Otsu, A threshold selection method from gray-level histograms, IEEE Transactions on Systems, Man, and Cybernetics 9 (1) (1979) 62–66, https://doi.org/10.1109/tsmc.1979.4310076.

Yanhua Bian is a PhD candidate at the Institute of Mechanics, Chinese Academy of Sciences, China. Her research interests include additive manufacturing, fused deposition modeling and selective laser melting.

Xiuli He is an associate professor at the Institute of Mechanics, Chinese Academy of Sciences, China. She received her PhD from the Pennsylvania State University, the United States. She is engaged in the research of additive manufacturing, welding and joining, and computational materials processing.

Gang Yu is a professor at the Institute of Mechanics, Chinese Academy of Sciences, China. He received his Ph.D. from Heriot-Watt University, the United Kingdom. His research focuses on laser advanced manufacturing and additive manufacturing technology.

Shaoxia Li is an associate professor at the Institute of Mechanics, Chinese Academy of Sciences, China. She holds a Ph.D. from the Institute of Mechanics, Chinese Academy of Sciences, China. Her research interests include additive manufacturing and laser surface modification.

Chongxin Tian is an assistant professor at the Institute of Mechanics, Chinese Academy of Sciences, China. His research interests include additive manufacturing and surface nanocrystallization of materials.

Zhiyong Li is an assistant professor at the Institute of Mechanics, Chinese Academy of Sciences, China. His research interest includes additive manufacturing, welding and joining.

Yanmei Zhang is currently studying for her master's degree at the Institute of Mechanics, Chinese Academy of Sciences, China. Her research interests include laser manufacturing, laser drilling and simulation of two-phase flow.

Junming Liu is an assistant professor at Research Institute of 3D printing, Beijing City University, China. Her research interests include additive manufacturing and numerical simulation.